Analysis and Prediction of Edge Effects in Laser Bending

Jiangcheng Bao

Y. Lawrence Yao

Department of Mechanical Engineering,
Columbia University,
New York, NY 10027

Laser forming of sheet metal offers the advantages of requiring no hard tooling and thus reduced cost and increased flexibility. It also enables forming of some materials and shapes that are not possible now. In single-axis laser bending of plates, the bending edge is found to be somewhat curved and the bending angle varies along the laser-scanning path. These phenomena are termed edge effects, which adversely affect the accuracy of the bending and result in undue residual stress. Numerical investigations are carried out to study the process transiency and the mechanism of the edge effects. Temperature dependency of material properties and strain-rate dependency of flow stress are considered in the numerical simulation to improve prediction accuracy. Numerical results are validated in experiments. Patterns of edge effects and resultant residual stress distributions are examined under a wide range of conditions. A more complete explanation for the mechanism of the edge effects is given. [DOI: 10.1115/1.1345729]

1 Introduction

Laser forming involves heating sheet metal workpiece along a certain path with a defocused laser beam directed normal to the surface, and with or without a jet stream of cold gas or water emulsion cooling the path after the beam passes. During laser forming, a transient temperature field is caused by the irradiation and traveling of a laser beam. Consequently, thermal expansion and contraction take place, which give rise to deformation of the workpiece. Laser forming has its roots in a traditional sheet metal forming method—flame bending, where the sheet metal is heated and deformed by an oxy-acetylene torch.

Laser forming has the following advantages over the traditional metal forming technologies. It requires no tools or external forces in the process. The cost of the forming process is greatly reduced compared with the traditional mechanical forming when small-batch production and prototyping of sheet metal components are concerned. With the flexibility of the laser beam delivering and numerical control system, it is easier to incorporate laser forming into an automatic manufacturing system. Material degradation in laser forming is typically limited to a very tiny layer of the irradiated surface due to highly concentrated beam power and short interaction time, and therefore laser forming may be used for materials that are sensitive to high temperature.

Efforts have been made to understand the mechanism underlying laser forming. Vollertsen [1] suggested that three kinds of mechanism exist in laser forming, namely temperature gradient mechanism (TGM), buckling mechanism (BM) and upsetting mechanism (UM). The TGM is dominant under conditions corresponding to a small Fourier number ($F_0 = \alpha \cdot t/s^2$, where α is thermal diffusivity, t characteristic time and s sheet thickness) or modified Fourier number ($F_0 = \alpha \cdot d/(s^2 \cdot v)$, where d is beam diameter at the workpiece surface and v traveling velocity). The BM dominates for a high Fourier number. Two characteristics of this mechanism are no steep temperature gradient along the sheet thickness direction and the extension of heated area compared to the sheet thickness. The UM is based on the increase of the sheet thickness and shortening of the sheet length. It is similar to the BM while the dimension of the heated area is much larger than that in the BM.

Most research work to date has been focused on straight-line laser bending (Fig. 1(*a*)), a simple form of laser forming. Analytical models have been derived to predict the bending angle in the

straight-line laser bending. A simple beam model was proposed based on the TGM assumption and an energy approach to the temperature field was used in Vollertsen's two layer model [2]. In terms of agreement with experimental results, this model is a great improvement compared with previous analytical models. However, it assumed that all input energy is used for plastic deformation, and ignores the energy dissipation due to reversed straining during cooling. Mucha et al. [3] modeled the TGM and provided solutions, by assuming different shaped plastic zones. This model helped determine the critical conditions for the TGM, but it can only be used to calculate the final bending angle, without insight into the transiency of the forming process, which is of great interest for understanding the underlying mechanism and realizing process control. By assuming a complete plastic zone in the area near the center of the beam, and a complete elastic zone in remote areas, Vollertsen et al. [4] established an analytical model for the BM. This model is valid only for high ratio of thermal conductivity to thickness, i.e., the heat conduction is basically 2D. This is, however, not always the case, especially when temperature gradient exists throughout the thickness direction.

To overcome the limitations of the analytical approach and generate more prediction capabilities, efforts have been made in numerical modeling. Alberti et al. [5] carried out a numerical simulation of the laser bending process by a coupled thermal mechanical analysis. Temperature dependency of flow stress was taken into consideration. Hsiao et al. [6] simulated the bending process by taking into account the convection and radiation boundary conditions, and using extrapolation for mechanical properties at higher temperature. Work hardening was not considered in Hsiao's model. Holzer et al. [7] modeled the bending process under the BM. An eight-node element was used, which is good for capturing the intensive temperature change, but not suitable for a bending-dominated deformation process such as laser bending. As temperature often rises very high in laser forming, temperature dependency of material properties becomes very important to the simulation accuracy. Large deformation is desired in laser forming, and consequently, it is necessary to consider strain hardening, especially in the case of multiple scan [8]. In order to obtain higher productivity, high traveling velocities are often employed in laser forming. In such cases, the strain rate could be high. Dependency of flow stress on the strain rate is much stronger at elevated temperatures.

Despite the progress made to date, there still exist problems that need to be addressed before laser forming becomes a practical processing technology. Among them are the geometrical accuracy and residual stress of laser formed components. In the straight-line laser bending, variation of the bending angle along the bending
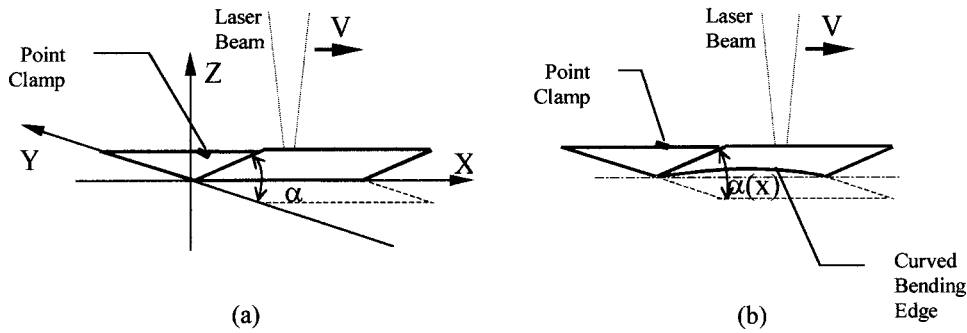

Fig. 1 Schematic of straight-line laser bending (*a*) showing no edge effects (*b*) showing edge effects characterized by the curved bending edge and non-uniform bending angle varying along the scanning path $\alpha(x)$

edge has been observed, as illustrated in Fig. 1(*b*). The bending edge is also somewhat curved. These two forms of inaccuracies together are termed as edge effects in this paper. The edge effects are obviously undesirable since they cause the deviation from the design intent (constant bending angle along the straight bending edge), cause a certain warpage of the component, and may cause additional residual stresses.

Magee et al. [9] showed that the extent of edge effects depends on the thermal diffusion from the laser beam into the entire plate, and the geometrical constraint of the workpiece as it varies with distance from the end point of the scanning path. The actual profile of bending angle is dependent on the laser processing parameters employed, as well as the material properties. Materials with very different thermal conductivity and expansion exhibited different variation patterns of the bending angle. Attempts have been made to reduce the edge effects by empirically varying the traveling velocity along the scanning path. Results showed that the varying velocity profile could lead to a sizable reduction of the edge effects.

Theoretical analysis by Mucha et al. [3] showed that thickness in the bending edge region increases due to thermal contraction under the TGM, and the bending edge of the plate is visibly curved due to thermal contraction in the scanning direction. Again, this analytical model does not describe the transient stage, while understanding of the transient stage is useful in analyzing the causes of the edge effects and realizing process control. Numerical and experimental attempts have been made by Bao and Yao [10] to study the edge effects. Preliminary investigation into the causes of the edge effects has been carried out. No residual stress was considered and no multiple mechanisms are considered.

This paper presents experimental and numerical investigations aimed at advancing the understanding of the causes of the edge effects in the straight-line laser bending process under a wide range of conditions. These conditions correspond to different forming mechanisms. Experimental results provide more laser forming data under different conditions and are used to validate the numerical results. Numerical results provide more insights into the causes of the edge effects, and help predict such effects on final dimensional accuracy and residual stress.

2 Numerical Simulation

In this study, temperature and strain-rate dependency of material properties is considered. Work hardening, though less significant in single scanning, is also considered in order to improve simulation and prediction accuracy.

2.1 Assumptions. The following assumptions are made for the numerical modeling.

The power density distribution of the laser beam follows a Gaussian function. The laser operates in CW mode. No cooling gas or water jet is employed.

Temperature dependency of material properties is considered, including thermal conductivity, specific heat, Young's modulus, Poisson ratio, and flow stress. Elastic strains are assumed to be much smaller than unity. The rate of deformation is the total strain rate, i.e., the sum of the elastic strain rate and plastic strain rate. Strain hardening of the material is considered through the strain-hardening coefficient, which is also temperature dependent. Dependency of flow stress on strain rate is modeled by defining a stress ratio $R(\theta, \dot{\varepsilon})$, the ratio of the flow stress at a certain strain rate to the static flow stress, as a function of temperature θ and strain rate $\dot{\varepsilon}$.

Dissipation of energy due to plastic deformation is negligible compared with the intensive energy involved. It is assumed that no melting is involved in the forming process.

2.2 Basic Relationships. The effective laser beam diameter of the Gaussian distribution is defined as the diameter at which the power density decreases to $1/e^2$, i.e., the power within the circular area given by this diameter is 95 percent of the total power input. The basic equation of energy balance is

$$\int_V \rho \dot{U} dV = \int_S q dS + \int_V r dV \qquad (1)$$

where V is the volume of a solid material with the surface area S, ρ the density of the material, $\dot{U}$ the material time rate of the internal energy, q the heat flux per unit area of the body flowing into the body, and r the heat supplied externally into the body per unit volume. By neglecting the coupling between mechanical and thermal problems, which is appropriate for laser bending where deformation does not change temperature in a significant way, internal energy U is related to temperature θ by specific heat $c(\theta) = dU/d\theta$, where θ is the temperature of the material, and U the internal energy of the material, which is dependent on the temperature only. Heat conduction is assumed to be governed by the Fourier law, i.e., heat flux is proportional to the temperature gradient, with thermal conductivity as the proportional constant.

Assuming isotropic linear elasticity for metallic materials, the stress, $d\sigma$, can be expressed as $d\sigma = K d\varepsilon_{kk} \delta_{ij} + 2G de_{ij}$, where K is the bulk modulus and G the shear modulus, which can be computed readily from Young's modulus E and Poisson's ratio v. Both Young's modulus E and Poisson's ratio v are temperature dependent, and so are bulk modulus K and shear modulus G. Von Mises criterion is used as the yield criterion, which is a pressure-independent yield criterion. It takes the following form in isothermal state $[(\sigma_1 - \sigma_2)^2 + (\sigma_2 - \sigma_3)^2 + (\sigma_3 - \sigma_1)^2]/6 = K^2$ where σ_1, σ_2 and σ_3 are principal stresses. K is determined by a uniaxial experiment, $\sigma_y^2/3 = K^2$ where σ_y is the yield stress in the uniaxial tension experiment. For plastic deformation, the govern-

ing rule is the flow rule, which is given by $d\varepsilon = d\lambda\,(\partial f/\partial\sigma)$ where f is a function of σ that describes the yield criterion. With the Von Mises criterion, the above equation becomes:

$$d\varepsilon_i = \frac{d\bar{\varepsilon}}{d\bar{\sigma}}\left[\frac{3}{2}\,\sigma_i - \frac{1}{2}\,\sigma_{kk}\right] \tag{2}$$

where $\bar{\varepsilon}$ is equivalent strain, $\bar{\sigma}$ is equivalent stress. Strain hardening describes the increasing of yield stress with the accumulation of plastic deformation. In laser forming process, though every point of the workpiece experiences a thermal cycle, the mechanical loading, however, as far as the plastic deformation is concerned, is essentially monotonic. Thus, the isotropic hardening rule is adopted. With work hardening, the flow stress is related to strain by $\sigma = K\cdot\varepsilon^n$, where n is strain-hardening coefficient, and can be found in literature. Strain-rate dependency of material properties is also taken into consideration by assuming that the flow stress is related with strain rate by the following equation $\sigma = D\cdot\dot{\varepsilon}^m$, where m is strain rate coefficient, and determined empirically [11]. For simplification, a ratio of yield stress to static yield stress, $R(\theta,\dot{\varepsilon})$, as a function of temperature θ and strain rate $\dot{\varepsilon}$, is defined as:

$$R(\theta,\dot{\varepsilon}) = \bar{\sigma}/\sigma^0 \tag{3}$$

where $\bar{\sigma}$ is yield stress after considering strain rate, and σ^0 the static yield stress. The thermal strain ε^{th} is related to a temperature matrix $\mathbf{T}$ by a linear coefficient of thermal expansion α. The energy balance model for deformation process follows:

$$\frac{d}{dt}\int_V (\rho\mathbf{v}\cdot\mathbf{v}/2 + \rho U)dV = \int_S \mathbf{v}\cdot\mathbf{t}\,dS + \int_V \mathbf{f}\cdot\mathbf{v}\,dV \tag{4}$$

where ρ is the current density, $\mathbf{v}$ the speed field vector, U the internal energy per unit mass, $\mathbf{t}$ the surface traction vector, $\mathbf{f}$ the body force vector, $\mathbf{n}$ the normal of boundary S, V the volume in study, and S the corresponding boundary surface.

2.3 Numerical Schemes. Since the heat transfer and elastic/plastic deformation are symmetric about the vertical plane containing the scanning path, only half of the plate is modeled in the numerical simulation. The same mesh model is used for the heat transfer analysis and structural analysis. In order to capture high gradients of temperature near the scanning path, a fine mesh is used in that region, while a coarse one is employed in remote areas.

A commercial code, ABAQUS, is used for the thermal mechanical simulation. In the structural analysis, the twenty-node element, $C3D20$, has no shear locking or hourglass effect, and is thus suitable for a bending-deformation-dominated process such as laser forming. On the other hand, the eight-node element suffers from ''shear locking,'' and is therefore not suitable for such a process. In order to keep compatible with the structural analysis, a twenty-node element, $DC3D20$, is used in the heat transfer analysis.

By standard Galerkin approach, Eq. (1) can be discretized in space:

$$\int_V N^N\rho\dot{U}dV + \int_V \frac{\partial N^N}{\partial\mathbf{x}}\cdot\mathbf{k}\cdot\frac{\partial\theta}{\partial\mathbf{x}}dV = \int_V N^N rdV + \int_{S_q} N^N qdS \tag{5}$$

where N is the nodal number. This set of equations is the ''continuous time description'' of the geometric approximation. With the backward difference algorithm

$$\dot{U}_{t+\Delta t} = \frac{U_{t+\Delta t} - U_t}{\Delta t}, \tag{6}$$

Eq. (5) can be discretized in time domain:

$$\frac{1}{\Delta t}\int_V N^N\rho(U_{t+\Delta t} - U_t)dV + \int_V \frac{\partial N^N}{\partial\mathbf{x}}\cdot\mathbf{k}\cdot\frac{\partial\theta}{\partial\mathbf{x}}dV - \int_V N^N rdV$$

$$- \int_{S_q} N^N qdS = 0 \tag{7}$$

This nonlinear system is then solved by a Modified Newton method.

2.4 Boundary Conditions. The laser beam is given as a prescribed nonuniform surface heat flux: $q = q(x,y,t)$ on the top surface. On five of the six boundary surfaces (except for the symmetric plane), free convection with air is considered: $q = h(\theta - \theta_0)$, where h is the heat transfer coefficient, and $\theta_0 = \theta_0(x,t)$ the surrounding temperature. Radiation is also considered on these five surfaces: $q = A((\theta - \theta_Z)^4 - (\theta_0 - \theta_Z)^4)$, where A is the radiation constant, and θ_Z the absolute zero on the temperature scale used. The symmetric plane is assumed to be adiabatic.

Two adjacent points in the middle of the symmetric plane are fixed in order to remove the rigid body motion. All other points within the symmetric plane are assumed to move only within the symmetric plane throughout the deformation process.

3 Experiment

The straight-line laser bending is schematically shown in Fig. 1. Figure 1(a) shows an ideal uniform bending angle α along the scanning path (defined as X-axis). The bending edge along the X-axis is not curved. The direction perpendicular to the scanning path and within the plate is defined as Y-axis. Figure 1(b) shows a more realistic case where the scanning edge is curved and the bending angle α varies with x.

The laser system used in the experiment is a PRC-1500 CO_2 laser, with a maximum output power of 1500 W. A coordinate measuring machine (CMM) is used to measure the bending angle at different positions along the scanning path. Coordinates of different points along the scanning edge are also measured, and the curvature of the scanning edge is subsequently calculated from these coordinates. The flatness of the unbent plates is measured using the CMM and the non-uniformity is smaller as compared with the final bending angle. A point clamp is used in the middle of one side of a workpiece (Fig. 1). Using the point clamp, one can better focus on the mechanism of the edge effects internal to the workpiece.

The experiment conditions are shown in Table 1. Material is low carbon steel, AISI1010. To enhance laser absorption by the workpiece, graphite coating is applied.

By holding the line energy constant, the input energy per unit length along the scanning direction is kept unchanged even though power and velocity change. Under conditions 1 to 3, the bucking mechanism (BM) is likely to dominate because of the large beam diameter to sheet thickness ratio. Under condition 5, the temperature gradient mechanism (TGM) is more likely to dominate because of the smaller beam-diameter to thickness ratio.

4 Results and Discussion

Experimental and numerical results under conditions 1 to 3 exhibit very similar trends and therefore only results under condition

Table 1 Experimental conditions

Condition No.	L.E. (J/mm)	P (W)	V (mm/s)	Size (mm^3)	d (mm)
1	20	200–1300	10–67.5	80×80×0.60	8
2	20	200–1300	10–67.5	80×80×0.89	8
3	30	200–1300	10–45	80×80×0.89	8
4	30	400–1000	13.3–33.3	80×76.3×1.5	8
5	20	800–1300	40–65	80×76.3×2.3	4

(L.E.=Line Energy, P=Power, V=Velocity, d=Beam Diameter)

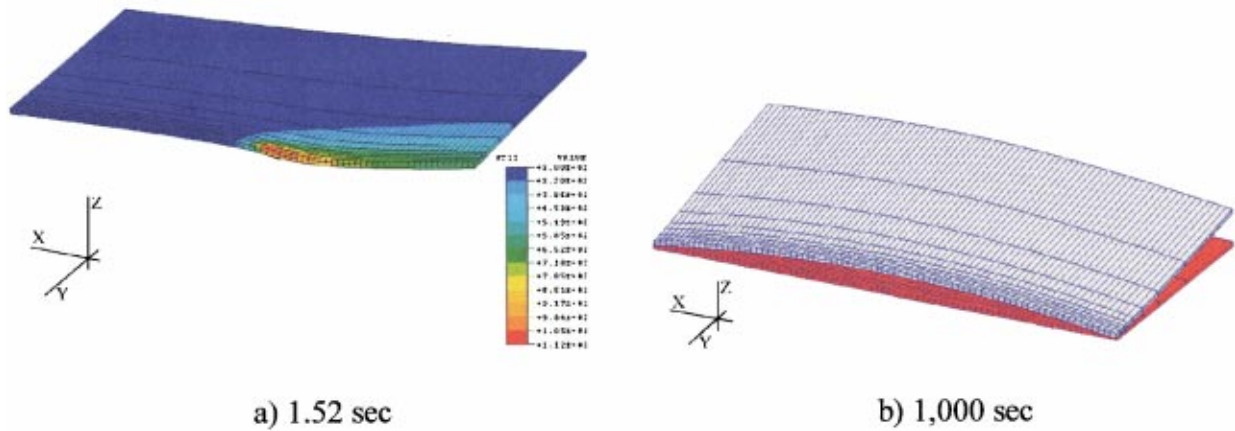a) 1.52 sec   b) 1,000 sec

Fig. 2 (*a*) **Temperature distribution in laser bending** (**deformation magnification 10X**)**, and** (*b*) **deformed compared with undeformed plate** (**deformation magnification 5X**) (**Half plate, condition 3, V=26.7 mm/s**)

3 are presented and analyzed in details. First, simulation results are validated by experimental measurements. Additional simulation results are then presented to help understand the process transiency and underlying mechanism of the edge effects. Finally, they are briefly compared with results under conditions 4 and 5.

4.1 Comparison of Experimental and Simulation Results. Figure 2 shows a typical thermal-mechanical simulation result where temperature distribution is superposed on deformation (magnified for easier visualization). Due to symmetry, only the half plate is simulated. As seen, it takes about three seconds to scan the 80-mm path at the velocity used, while deformation does not complete till much later. A curved bending edge is seen at 1,000 seconds. Figure 3 shows both experimental and simulation results of the bending angle along the scanning path and they agree with each other quite well. It can be seen that, from the entering end of the scanning path ($X=0$), the bending angle either drops a little and then increases or directly increases towards the exiting end, where the maximum value occurs.

Figure 4(*a*) shows the average bending angle vs. velocity. It can be seen that, despite the fact that the line energy is held constant, the average bending angle increases with velocity. Shown in Fig. 4(*b*) is the curvature of the bending edge vs. velocity. Figure 4(*c*) and (*d*) show comparison of experimental and numerical results of bending angle variation and relative bending angle variation, respectively. The bending angle variation is defined as the difference between the maximal and minimal bending angle along the

Fig. 3 Bending angle variation along the scanning path, $\alpha(x)$ (**Condition 3**)

bending edge for a given condition. The relative bending angle variation is the ratio of the bending angle variation to the average bending angle.

Generally speaking, the simulation results agree quite well with the experimental results. Not only the average bending angle and curvature, but also the bending angle variations along the scanning direction are relatively well captured by the numerical model. As mentioned before, the bending angle variation (Fig. 4(*c*)) and curved bending edge (Fig. 4(*b*)) together are termed edge effects in this paper. Similar results are obtained under conditions 1 and 2.

4.2 Edge Effects. To help understand the causes of the edge effects as seen in Figs. 3 and 4, additional numerical results are shown in Figs. 5–7. The peak temperature that points on the top surface along the scanning path typically experienced is shown in Fig. 5(*a*). Apparently, the much higher peak temperature at the exiting end is attributed to the reduced heat dissipation near the exit boundary. Figure 5(*b*) is a typical time history of temperature at the top and bottom surfaces along the scanning path for two different scanning velocities but at the same line energy. As seen, temperatures are higher at the higher velocity due to less time for heat dissipation. At the higher velocity, the difference between the peak temperature at the top and bottom surfaces is also larger than that at the lower velocity for the same reason.

Despite the fact that the line energy is held constant, the average bending angle increases with velocity (Fig. 4(*a*)). This is mainly due to the fact that, at higher velocities, temperatures are higher because of less energy dissipation and temperature difference between the top and bottom surfaces is greater (Fig. 5(*b*)). The fact that the temperature at the exit point is much higher than that at the entrance point (Fig. 5(*a*)) explains why the bending angle at the exit point differs from that at the entrance point (Fig. 3). This is one reason why the bending angle is not uniform along the scanning direction. The other cause for the bending angle variation is the curved bending edge (Fig. 4(*b*)), which will be explained below.

The bending angle variation (Fig. 4(*c*)), defined as the difference between the maximal and minimal bending angle along the scanning direction for a given operation, rises quickly first, peaks at about 20 mm/s, and then levels off or slightly decreases with the increase of velocity. The curvature of the bending edge also starts to decrease in slope significantly at around 20 mm/s (Fig. 4(*b*)). It therefore seems reasonable to conclude that the curved bending edge is another reason for the bending angle variation to occur along the scanning direction.

The cause of the curved bending edge is in turn due to the difference in the *X*-axis contraction between the top and bottom
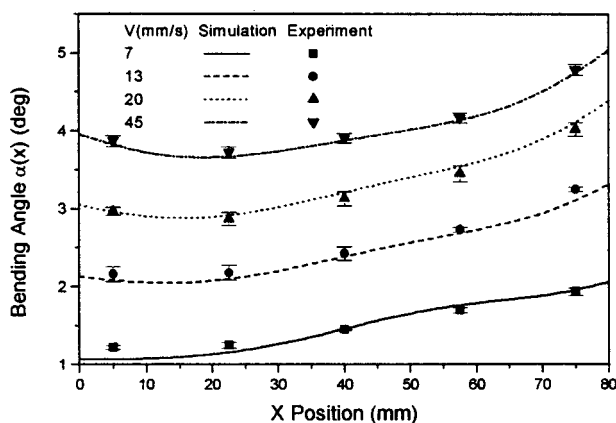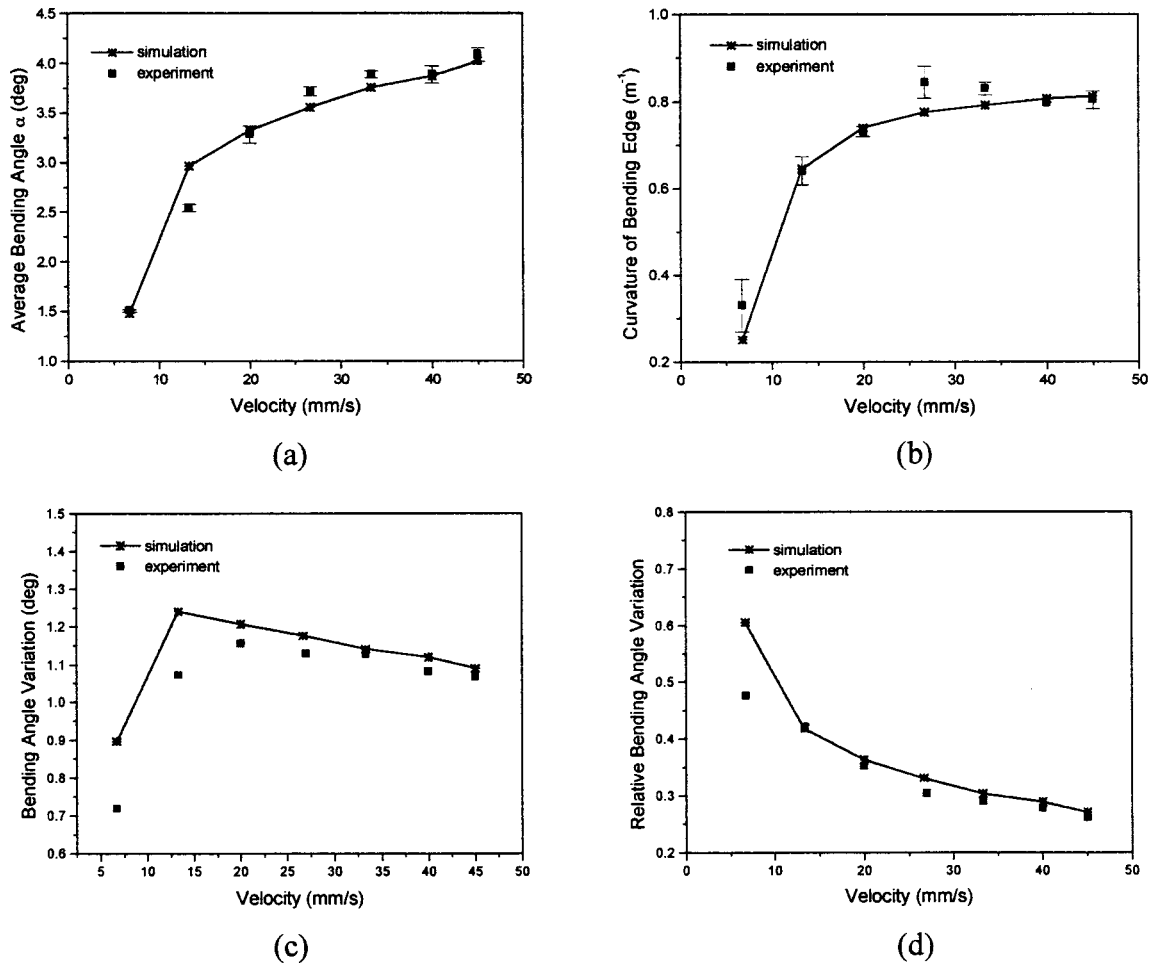
Fig. 4 Comparison of simulation and experiment under condition 3 (*a*) average bending angle, (*b*) curvature of the bending edge, (*c*) bending angle variation (difference between the max and min), and (*d*) relative bending angle variation (bending angle variation vs. average bending angle)

surfaces (Fig. 6). Figure 6(*a*) shows the simulation result of contractions in the *X* direction on the top and bottom surfaces along the scanning direction. Figure 6(*b*) shows the difference of the two contractions. The simulation result of the bending edge curvature in Fig. 4(*b*) is also superposed here for the convenience of discussion. To further explain the *X*-axis contraction and the reason for the difference, the time history of plastic strains at a typical location on the scanning path ($X = 20$ mm) is examined in Fig. 7. Figure 7(*a*) shows the time history of the plastic strain on the top surface of that location (in three perpendicular directions). Figure 7(*b*) shows the time history of the *X*-axis plastic strain on the top and bottom surfaces at the same location. Near the top layer along the scanning path, compressive strain occurs in the *X* and *Y* directions and tensile strain in *Z* direction (Fig. 7(*a*)). Please note the sum of these plastic strains is zero at any given time based on the assumption of constant volume in plasticity [12]:

$$d\varepsilon_1 + d\varepsilon_2 + d\varepsilon_3 = 0 \qquad (8)$$

where ε_1, ε_2 and ε_3 are strains in three mutually perpendicular directions. During the rapid heating stage (at around one second seen in Fig. 7), a significant *Y*-axis compressive plastic strain occurs due to the great geometric constraint of the workpiece in that direction while the tensile plastic strain in the *Z* direction occurs freely due to the much less constraint in the thickness direction. Less well known is the compressive plastic strain in the *X* direction, which is also caused by the geometric constraint of the plate in that direction although the constraint is not as great as that in the *Y* direction. The bottom surface along the scanning path un-

dergoes a very similar plastic deformation process as the top surface, except the magnitude is smaller. This is understandable because under condition 3, the buckling mechanism is dominant and thus the temperature difference between the top and bottom surface is moderate. A comparison between the plastic strains at the top and bottom surfaces is shown in Fig. 7(*b*). Figure 7(*b*) also shows that, during the cooling stage (after about one-second seen in Fig. 7), the reverse of the *X*-axis compressive plastic strain at the top surface is more than that at the bottom surface. This is because, during the cooling stage, the top surface undergoes more *Y*-axis compressive plastic strain (Fig. 7(*a*)) than that at the bottom surface. Based on the constant volume assumption, the *X*-axis compressive plastic strain at the top surface reverses more than that at the bottom surface (Fig. 7(*b*)). Therefore, the total *X*-axis contraction near the bottom layer is larger than that near the top layer (Fig. 6). Consequently, the bending edge is curved away from the laser beam (Figs. 1 and 2).

As seen in Fig. 6(*b*), the greater is the difference between the contractions near the top and bottom surfaces, the greater the curvature. The fact that the curvature increases with velocity can be explained by the increase in average bending angle with velocity. Obviously, when the average bending angle is larger, the above-mentioned difference between the top and bottom surfaces will be more pronounced, and therefore the curvature will be greater. As seen from Figs. 4(*a*) and (*b*), at higher velocities where the average angles are larger, the curvatures of the bending edge are also greater.
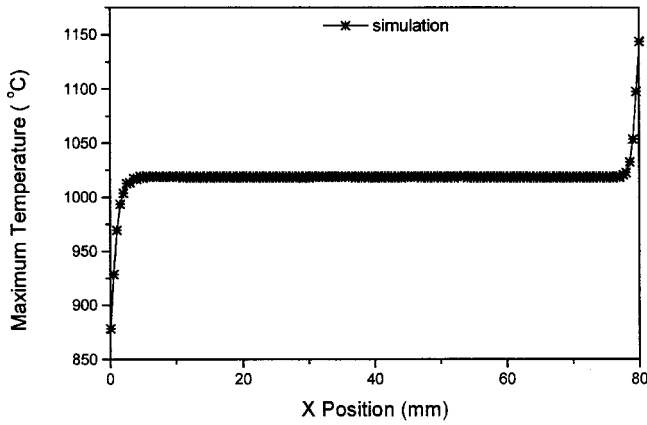
(a)
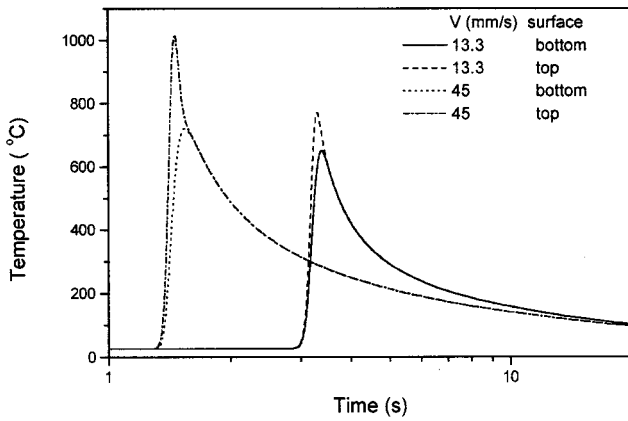
(b)

Fig. 5 (*a*) **Typical peak temperature reached on the top surface along the scanning path (Condition 3, *V*=45 mm/s), and** (*b*) **temperature history of a typical point on the scanning path (Condition 3, *V*=13.3 and 45 mm/s)**

4.3 Residual Stress. Residual stress affects such important materials design properties as fatigue life, fracture strength, and onset of yield. To study the residual stress, Fig. 8 shows a typical *Y*-axis plastic strain, elastic strain and residual stress distribution at the top, middle and bottom layers along the scanning path. As seen from Fig. 8, the plastic strain near both ends of the scanning
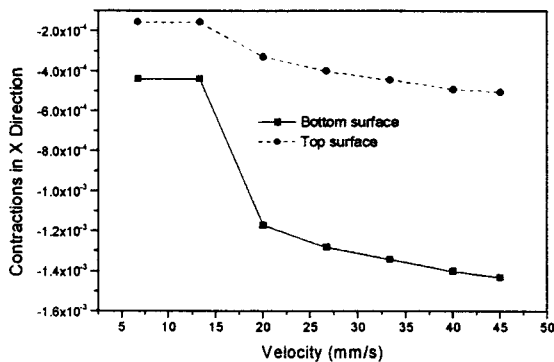
path is small because of the reduced geometric constraint of the plate in these regions, while along the rest of the scanning path significant compressive plastic strain is seen. This clearly explains why the residual stress is compressive at both ends and tensile along the rest of the scanning path.

It is worth noting that the difference in the plastic strain between the top and bottom surfaces at a location, say, $X = 20$ mm, is smaller than that at a location, say, $X = 60$ mm. This is because, before the laser beam reaches the location at $X = 60$ mm, a certain amount of compressive plastic strain near the top surface and tensile plastic strain near the bottom surface have already accumulated at the location due to the bending taking place at the preceding regions on the scanning path. This also explains why the bending angle at $X = 20$ mm is smaller than that at $X = 60$ mm (Fig. 3).

As seen in Fig. 8, the profile of the residual stress distribution is understandably very similar to that of the elastic strain distribution. The small shift along the vertical axis is governed by the relationship for isotropic elasticity, that is,

$$E_{22} = \frac{1}{E_Y}[T_{22} - \upsilon(T_{33} + T_{11})] \qquad (9)$$

where E_{22} is the elastic strain in the Y direction, T_{11}, T_{22} and T_{33} are stress in the X, Y and Z direction, respectively. In this case, $T_{33} \approx 0$, and T_{11} is small as compared with T_{22}. Shown in Fig. 9 is the contour plot of the Y-axis residual stress along the scanning path and within the symmetric plane.

4.4 Other Conditions. So far, our discussion has been focused on condition 3 where the buckling mechanism (BM) of laser forming dominates. Under the condition, the edge effects are characterized by a concave bending angle variation (Fig. 3) and the scanning edge is curved away from the laser. Similar results are obtained in experiments and simulation under conditions 1 and 2. Under conditions 4 and 5, however, the BM may not dominate. In fact, under condition 5, the temperature gradient mechanism (TGM) dominates due to the reduced beam diameter and increased plate thickness. Condition 4 represents the situation where the BM transits to the TGM or the BM and TGM co-exist. As a result, the edge effects exhibit patterns different from condition 3. As seen from Fig. 10(*a*), the bending angle variation measured along the scanning path is almost linear under condition 4. Experimental and simulation results show the bending angle variation is convex under condition 5 (Fig. 10(*b*)). In addition, the scanning edge is curved towards the laser under condition 5 as opposed to curving away from the laser under condition 3.

The time history of the *X*-axis contraction for conditions 3 and 5 is plotted in Fig. 11. As seen from Fig. 11(*a*), the top and bottom
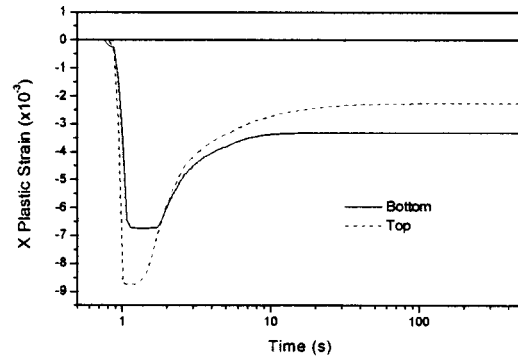

(a)
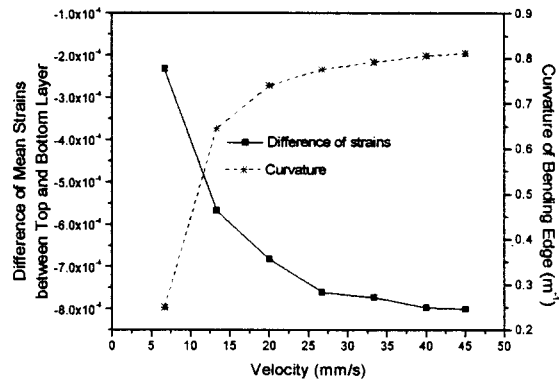
(b)

Fig. 6 (*a*) **Contractions in the scanning direction (X-axis), and** (*b*) **difference of mean strains between the top and bottom layer along the X-axis and curvature of the bending edge (Condition 3)**
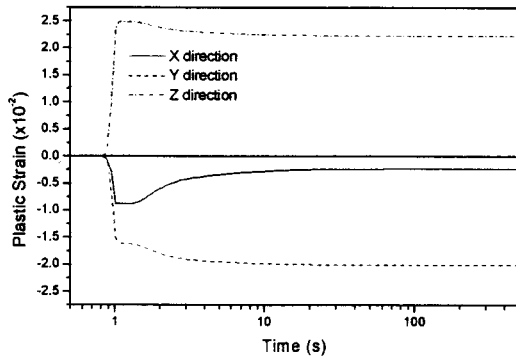
Fig. 7 Time history of plastic strain for a typical point (X=20 mm) (*a*) X-, Y-, and Z-axis plastic strain on the top surface along the scanning path, and (*b*) X-axis plastic strain on the top and bottom surfaces along the scanning path (Condition, 3, V=26.7 mm/s)

layers experience similar contraction during the heating stage for the BM-dominated bending operation (condition 3) where temperature difference between the top and bottom surfaces is moderate. But the bottom layer contracts more than the top layer dur-

Fig. 8 Y-axis plastic strain, elastic strain and residual stress along the scanning path (Condition, 3, V=26.7 mm/s)

ing the cooling stage because the *Y*-axis contraction at the top surface is greater than that near the bottom surface. This leads to a bending edge curved away from the laser.

For the TGM-dominated bending operation where the temperature difference between the top and bottom layers is much greater (condition 5), the top layer contracts more than the bottom layer during the cooling stage (Fig. 11(*b*)) simply because the temperature gradient in the thickness direction dominates. Shown in Fig. 12 is the contour plot of the *Y*-axis residual stress for condition 5. As seen, the top and bottom layers are tensile and the middle layer is compressive, which is typical for the TGM-dominated bending operation.
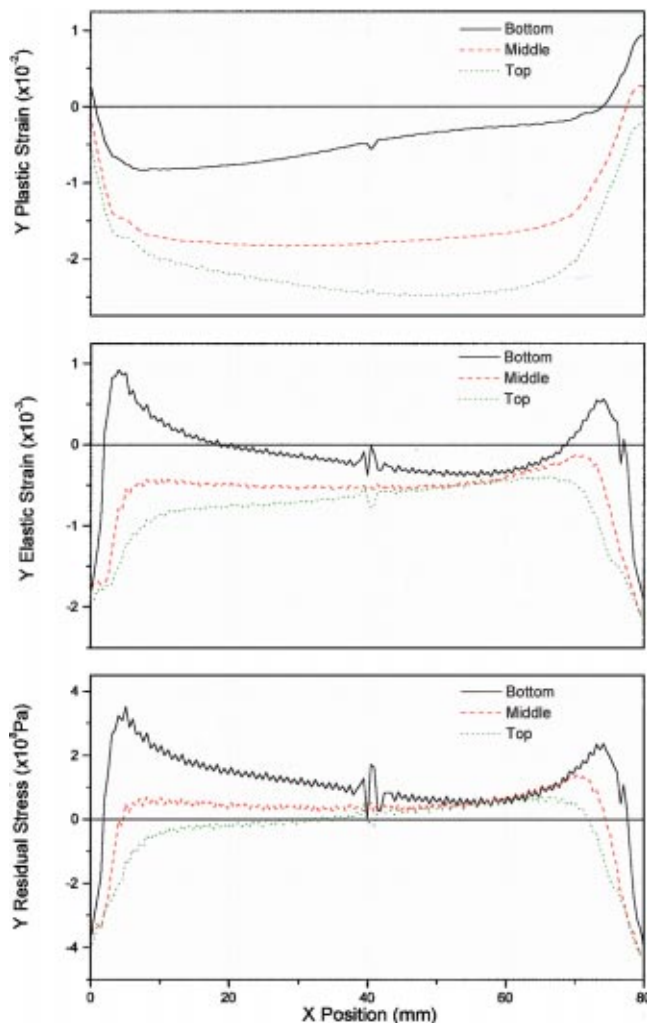
5 Conclusions

Numerical results agree quite well with experimental results. Not only the average bending angle and the curvature but also the bending angle variation can be reliably predicted. This is indicative of the reasonableness and comprehensiveness of the assumptions made in the numerical modeling for the conditions under which the investigation was carried out.

Both numerical and experimental results confirm that edge effects are characterized by a concave pattern in the bending angle variation along the scanning path and a bending edge curved away from the laser under conditions 1 to 3, where the forming process
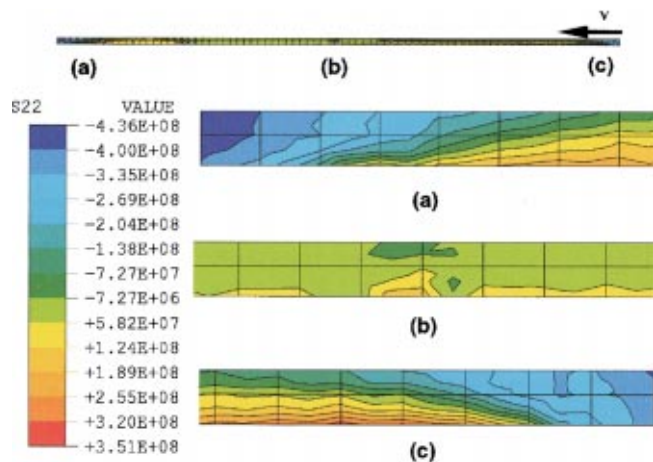

Fig. 9 Contour plot of Y-axis residual stress along the scanning path and within the symmetric plane (Condition 3, V=26.7 mm/s)
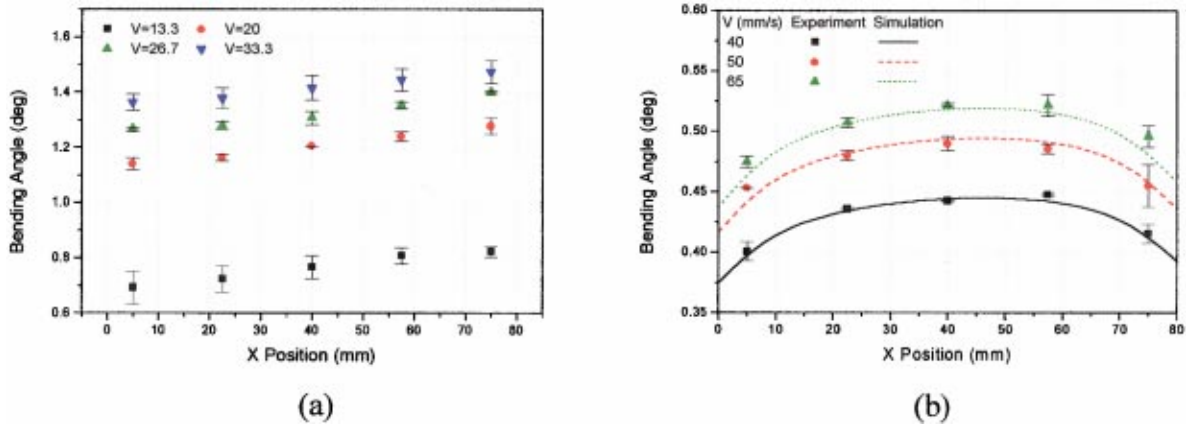
Fig. 10 (*a*) **Measurement of bending angle** $\alpha(x)$ (**Condition 4**), **and** (*b*) **simulation and experimental results of bending angle** $\alpha(x)$ (**Condition 5**)
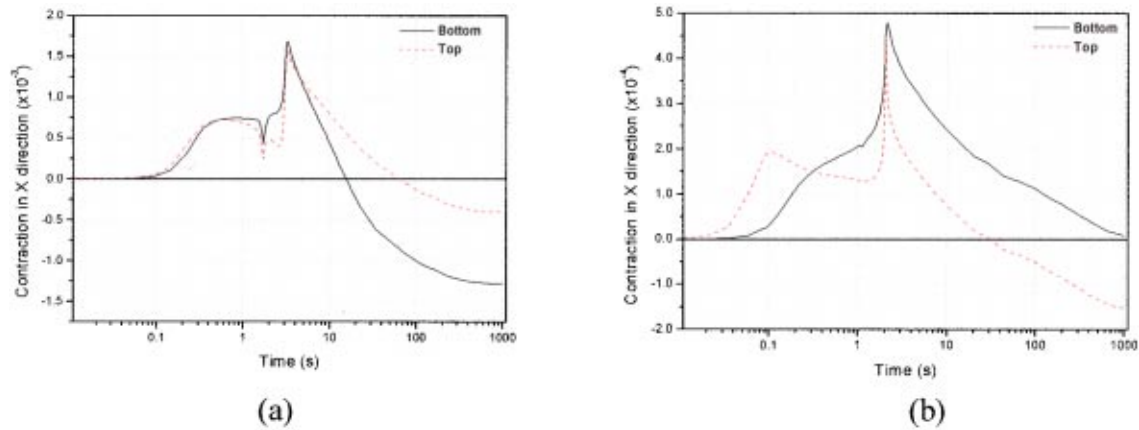

Fig. 11 Time history of X-axis deformation (*a*) **condition 3** (**Buckling mechanism dominated**), **and** (*b*) **condition 5** (**Temperature gradient mechanism dominated**)
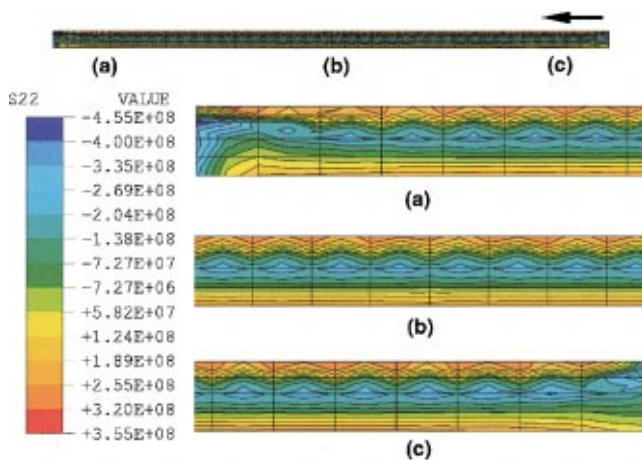

Fig. 12 Contour plot of Y-axis residual stress along the scanning path and within the symmetric plane (**Condition 5, V =26.7 mm/s**)

is dominated by the BM. Results from simulation and experiments also show that under condition 5 where the TGM dominates, the pattern of edge effects is different, which is characterized by a convex bending angle variation and the bending edge curved towards the laser.

In the case of the BM-dominated bending operation, the X-axis contraction near the bottom surface is more significant than that near the top surface, resulting in a bending edge curved away from the laser, while the opposite is true in the case of the TGM-dominated bending process. The observation of a convex or concave pattern of the bending angle variation is closely related with the direction of the curved bending edge. The improved understanding and prediction capabilities of the edge effects will facilitate process planning and control.

Acknowledgments

References

[1] Vollertsen, F., 1994, ''Mechanisms and Models for Laser Forming,'' *Laser Assisted Net Shape Engineering, Proceedings of the LANE'94*, Vol. 1, Meisenbach Bamberg, pp. 345–360.
[2] Vollertsen, F., 1994, ''An Analytical Model for Laser Bending,'' Lasers Eng., **2**, pp. 261–276.

[3] Mucha, Z., Hoffman, J., Kalita, W., and Mucha, S., 1997, ''Laser Forming of Thick Free Plate,'' *Laser Assisted Net Shape Engineering 2, Proceedings of the LANE'97*, Meisenbach Bamberg, pp. 383–393.

[4] Vollertsen, F., Komel, I., and Kals, R., 1995, ''The Laser Bending of Steel Foils for Microparts by the Buckling Mechanism—A Model,'' Modell. Simul. Mater. Sci. Eng., **3**, pp. 107–119.

[5] Alberti, N., Fratini, L., and Micari, F., 1995, ''Numerical Simulation of the Laser Bending Process by a Coupled Thermal Mechanical Analysis,'' *Laser Assisted Net Shape Engineering, Proceedings of the LANE'94*, Vol. 1, Meisenbach Bamberg, pp. 327–336.

[6] Hsiao, Y.-C., Maher, W., et al., 1997, ''Finite Element Modeling of Laser Forming,'' *Proc. ICALEO'97*, Section A, pp. 31–40.

[7] Holzer, S., Arnet, H., and Geiger, M., 1994, ''Physical and Numerical Modeling of the Buckling Mechanism,'' *Laser Assisted Net Shape Engineering, Proceedings of the LANE'94*, Vol. 1, Meisenbach Bamberg, pp. 379–386.

[8] Sprenger, A., Vollertsen, F., Steen, W. M., and Waltkins, K., 1994, ''Influence of Strain Hardening on Laser Bending,'' *Laser Assisted Net Shape Engineering, Proceedings of the LANE'94*, Vol. 1, Meisenbach Bamberg, pp. 361–370.

[9] Magee, J., Watkins, K. G., Steen, W. M., Calder, N., Sidhu, J., and Kirby, J., 1997, ''Edge Effects in Laser Forming,'' *Laser Assisted Net Shape Engineering 2, Proceedings of the LANE'97*, Meisenbach Bamberg, pp. 399–408.

[10] Bao, J., and Yao, Y. L., 1999, ''Study of Edge Effects in Laser Bending,'' *1999 International Mechanical Engineering Congress and Exposition*, MED 10, Nov. 14–19, 1999, pp. 941–948.

[11] Li, W., and Yao, Y. L., 2000, ''Numerical and Experimental Study of Strain Rate Effects in Laser Forming,'' ASME J. Manufacturing Science and Engineering, **122**, August, pp. 445–451.

[12] Mielnik, E. M., 1991, *Metalworking Science and Engineering*, McGraw-Hill, New York.